Journal of Materials Chemistry A

ROYAL SOCIETY OF CHEMISTRY

PAPER

View Article Online
View Journal | View Issue

Cite this: J. Mater. Chem. A, 2026, 14, 11395

Understanding dissolution mechanism of oxide perovskites and activity tuning for O_2 evolution by surface doping

Shagun Singh and Naiwrit Karmodak *

The oxygen evolution reaction (OER) is the major bottleneck in electrochemical water splitting. Development of efficient electrocatalysts from earth-abundant materials is essential. This study reports a design principle for tuning the catalytic efficiency and stability of perovskite oxides (ABO_3), focusing on $SrMnO_3$, $SrFeO_3$, $SrCoO_3$, and $SrNiO_3$ through B-site surface doping with Mn, Fe, Co, and Ni metal ions. Owing to multiple active sites and tunable oxidation states, these oxide surfaces exhibit a considerable reduction in thermodynamic overpotential (η_{TD}) upon doping. The dissolution free energy calculations are performed across a wide pH window (acidic to alkaline) and oxidative potentials to determine the Pourbaix stability and surface dissolution pathways. We find that $SrCoO_3$ and $SrNiO_3$ show the highest stability on doping with different transition metal atoms. Reaction free energy analysis indicates that the lattice oxygen mechanism generally outperforms the adsorbate evolution mechanism on the undoped surfaces. Surface doping results in a wide variation in the preferred reaction pathway. Mn-doped $SrNiO_3$ emerges as the most active system with η_{TD} of 0.34 V, while Fe doping enhances the activity of $SrCoO_3$ the most. Crystal orbital Hamilton population and electronic structure analyses show that modulation of the d-band center and surface structure deformation upon doping, influences the catalytic activity and stability. Using the activity descriptor $G_{max}(\eta)$ at an applied η of 0.3 V, the corresponding rate-determining steps (RDS) are identified. While most sites follow a single-step RDS, Fe- and Co-doped $SrNiO_3$ exhibit multistep contributions. On varying the doping percentages of Fe on the $SrCoO_3$ surface, we find that 25% surface doping shows the highest catalytic activity for OER.

Received 10th September 2025
Accepted 19th January 2026

DOI: 10.1039/d5ta07376f

rsc.li/materials-a

Introduction

With the depletion of fossil fuels and the enhancement of environmental pollution, the demand for clean and sustainable energy sources has surged significantly in recent years. Renewable energy generation from solar, wind, and hydro power has shown significant advantages.[1] However, these renewable energy options often face challenges due to seasonal natural cycles and regional variability. To address these limitations, there has been growing interest over the past few decades in developing energy storage and conversion technologies to store energy intermittently and use it as needed.[2–5]

The water-splitting reaction could allow for the generation of renewable fuels.[6–8] Electrochemical water-splitting reactions involve two half-cell reactions: the hydrogen evolution reaction (HER: $2H^+ + 2e^- \rightarrow H_2$) at the cathode and the oxygen evolution reaction (OER: $2H_2O \rightarrow O_2 + 4H^+ + 4e^-$) at the anode.[3,9–11] H_2 serves as a clean fuel but while the formation of H_2 is more important, the OER at the anodic half-cell is the primary bottleneck of the process. The high overpotential associated with the OER reduces the overall reaction efficiency.[12–16]

An efficient electrocatalyst could reduce the overpotential for O_2 evolution. In the past decades, increasing attention has been given to developing electrocatalysts for OER. While developing efficient catalysts, three crucial factors must be considered: activity, stability, and cost-effectiveness.[1,17–20] The Pt-group metal-based electrocatalysts, such as iridium oxide (IrO_2) or ruthenium oxide (RuO_2), are found with the highest efficiency in an acidic medium for the OER.[21–23] However, due to their expensive nature, these catalysts would be unsuitable for industrial-scale utilization. The other catalysts with good activity for OER face several inherent challenges. The catalytic surfaces undergo surface reactions under applied potentials and solvent pH, resulting in the gradual degradation of the catalytic sites.[24–29] This leads to a reduction in the catalytic efficiency under operating conditions over time. Inspired by the recent advancements in developing effective synthetic strategies and understanding catalytic efficiencies of transition metal-based catalysts, tremendous research attention has been

Department of Chemistry, Shiv Nadar Institution of Eminence, Greater Noida, India, 201314. E-mail: naiwrit.karmodak@snu.edu.in

drawn to investigate the OER activity of the transition metal oxide surfaces.[30–34]

Transition metal oxides have emerged as a promising alternative to traditional Pt-group metal-based electrocatalysts for OER. Among these, perovskite oxides, with the general formula ABO_3, offer unique advantages.[35–41] Typically, the A-site is occupied by non-transition metal ions, whereas the B-site hosts transition metal ions. The A-site shows the 12-fold coordination with oxygen, and the B-site has a 6-fold coordination.[34,35] The oxidation states of the transition metal site in perovskite oxides could be further tuned by varying the A-site metal ions and the creation of the O vacancies.[42–44] Furthermore, in recent studies, precise synthetic techniques have been developed for precisely doping the B-site metal ions, with multiple transition metals with varying oxidation states. This flexibility could allow for precisely modulating the catalytic properties.[32,32,34,45–53]

In addition to catalytic activity, stability is a crucial factor in evaluating the efficiency of an electrocatalyst.[26–29] The perovskite oxide catalysts show a performance degradation often linked with the surface oxidation and aqueous dissolution.[9,54] To enhance the surface activity and stability under the OER environment, strategies such as doping with different transition metals have been employed for spinel and antispinel oxide surfaces.[55] Bimetallic and multi-metallic spinel oxide surfaces show multiple active sites with tunable oxidation states.[56–63] Furthermore, the presence of different metal centers with varying electronegativity helps in redistributing the metal–O electron density and improves the resistance to aqueous dissolution under various oxidative electrochemical conditions.[58,64–67]

Recent studies have reported several oxide perovskite materials with comparable activity for OER as the Pt-group metal-based catalysts.[32,32,50–53] The electrochemical stability of the perovskite oxides have been a major issue retarding the electrochemical activity for OER.[9,54] Understanding the aqueous dissolution pathways of the oxide perovskite surfaces will allow devising an effective approach to improve their electrocatalytic activity for OER and unleash a design principle. The OER activity of perovskite oxides is closely linked to their electronic structure and frontier energy states, pinning near the Fermi energy level.[9,32,34,45,49–53,68] The frontier energy states could also regulate the surface reactivity with the aqueous environment. Therefore, a strategy to modulate the frontier energy states will lead to an optimum strategy to tune both the activity and stability of these surfaces. Inspired by this idea, in this study, we employ a B-site surface doping of the four perovskite oxides surfaces ($SrMnO_3$, $SrFeO_3$, $SrNiO_3$, and $SrCoO_3$) with different transition metal atoms (Mn, Fe, Ni, and Co).[46,69,70] Modulating the d-band center of the oxide surfaces, we tune the stability and electrocatalytic activity for the OER.[71] The surface Pourbaix analysis has been performed to understand the surface aqueous dissolution reactions and stable surface configurations under the oxidative potentials and varying pH from acidic to alkaline domains. Doping with transition metals is found to enhance the stability and activity of the surfaces of both $SrCoO_3$ and $SrNiO_3$. We find that $SrCoO_3$ with Fe-dopant and $SrNiO_3$ with Mn-surface dopant, the OER overpotential is considerably reduced compared to the undoped surfaces.

Computational details

The computational calculations are performed with density functional theory (DFT), using the Vienna *Ab initio* Simulation Package (VASP).[72–74] The electron exchange–correlation effects are treated within the Generalized Gradient Approximation (GGA) using the revised Perdew–Burke–Ernzerhof (RPBE) functional.[75] The projector augmented-wave (PAW) method[76] is employed to describe the electron–ion interactions, and a plane-wave basis set with an energy cutoff of 400 eV is used. The Brillouin zone is sampled using a $2 \times 2 \times 1$ Monkhorst–Pack *k*-point mesh.[77]

The electronic and ionic convergence criteria are set to 10^{-6} eV for energy and 10^{-3} eV Å^{-1} for forces, respectively. To account for non-covalent interactions between adsorbates and surfaces, van der Waals corrections are included. Solvent effects are incorporated using an implicit solvation model as implemented in the VASPSol package.[78–80] The implicit solvation model is employed to describe the electrochemical interface. In this setup, the perovskite surfaces and adsorbed intermediates are treated quantum mechanically, while the aqueous environment is represented by a polarizable continuum (PC) medium with a dielectric constant of 80. Electrolyte interactions are incorporated through a linearized Poisson–Boltzmann approach, with a Debye screening length of 3 Å. Non-electrostatic contributions to the solvation free energy arising from surface tension are excluded, as they are less significant in interfacial two-dimensional systems.[81,82] Consequently, the TAU parameter, which corresponds to the effective surface tension (eV Å^{-2}) in the VASPsol package and accounts for cavity formation free energy, is neglected in the present calculations.

All calculations are performed with spin polarization to account for the unpaired electron and variable spin states of the surface systems. The Atomistic Simulation Environment (ASE) package is used for generating VASP input files and post-processing of the computational results.[83] We have considered a 2×2 supercell of the perovskite surfaces to carry out the reaction free energy calculations. On the other hand, for the surface Pourbaix analysis, we have considered both 2×2 and 2×3 supercells of the surfaces to obtain the different surface vacancy structures. In all the simulations, a four-layer surface has been taken, with the bottom two layers kept fixed to mimic the bulk configuration. The upper two layers, along with the adsorbates, are allowed to minimize to obtain the most preferred geometries. A gap of 20 Å is kept along the non-periodic direction to minimize the furious interactions between the adjacent periodic cells. A detailed explanation of the computational method for reaction free energy and surface Pourbaix energy calculations is given in Sections S-I and S-II of the SI, respectively.[71]

Results and discussion

We perform the dissolution free energy calculations of the four perovskite oxides ($SrMnO_3$, $SrFeO_3$, $SrCoO_3$, and $SrNiO_3$), varying the pH from the acidic to alkaline range and the potential in the oxidative region from 1 to 2.0 V *vs.* SHE to

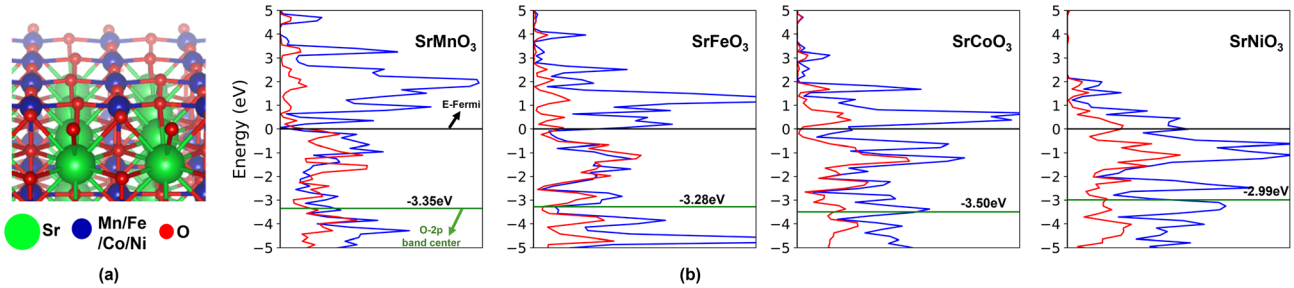

Fig. 1 (a) A schematic overview of the (001) surface termination of the pristine surface of oxide perovskite, where green spheres denote Sr, blue corresponds to the transition metal (Mn, Fe, Co, or Ni), and red spheres represent oxygen atoms. (b) The projected density of states (PDOS) plot for the (001) surfaces of $SrMnO_3$, $SrFeO_3$, $SrCoO_3$, and $SrNiO_3$. In these plots, the red regions correspond to the energy states of the O p-bands, while the blue regions represent the metal d-band states. The green horizontal line marks the O p band center with respect to the Fermi energy (black horizontal line).

understand the dissolution mechanism.[9] The corresponding stability is determined under varied electrochemical environments. In this study, we have considered the 001 surface termination with B-site ions on the surfaces. The 001 BO-site terminated (Fig. 1a) surfaces have been identified as the most stable surface terminations in the previous studies.[13,39,84–86] Furthermore, the 001 surfaces have been analyzed and found to be most active for OER. Therefore, we have built our model surfaces using the 001 BO surface terminations for the stability and catalytic studies.

Electrochemical stability of the pristine and doped 001 surface

Depending upon the positioning of the O-p band center with respect to the Fermi level (E_{Fermi}), the perovskite oxides show different dissolution pathways.[9] Fig. 1b shows the projected density of states (PDOS) of the 001 surface of the four perovskite oxides. The red region shows the energy states of the O-p bands. The O-p band center (denoted by the green line) is positioned relatively away from the E_{Fermi} for all the surfaces (varying within the range 2.99 to 3.50 eV). Therefore, based on previous studies, the dissolution mechanism will primarily involve the leaching of surface B-site transition metal ions.[54] Furthermore, on the 001 surfaces, the transition metal ions are in direct contact with the aqueous medium compared to the cationic Sr^{2+} ions; therefore, leaching of the surface transition metals will be more feasible than the A-site ion leaching.

The dissolution free energies (ΔG_{pbx}) for the transition metal ions are computed considering the stable transition metal ion phase separation to metal oxides at different oxidation states, as shown in eqn (1) (Section S-II in the SI gives a detailed overview of the calculation method):

$$SrMO_3 + zyH_2O \rightarrow SrM_{1-y}O_3 + yMO_z + 2zyH^+ + 2zye^- \quad (1)$$

Here, M corresponds to the transition metal ions, and y denotes the proportion of the metal ions leaching out from the surface. We have compared the stability of the surfaces with respect to the formation of different metal oxide solid phases (MO_z, where z determines the oxidation state of M in MO_z phases) after dissolution. The more negative the value of ΔG_{pbx}, the greater the possibility of dissolution. The ΔG_{pbx} values are calculated considering the surface vacancy formation of 17%, 25%, 33%, 50%, and 66%.

The ΔG_{pbx} for the four perovskite 001 surfaces is shown in Fig. 2(a)–(d) at three different pH levels. The y-axis corresponds to the ΔG_{pbx} values, and the x-axis denotes the variation in the oxidative potential with reference to SHE (V_{SHE}). The stable configurations are found to vary considerably depending on the potential ranges at each pH. The black vertical dotted lines give the potential ranges when we found a stability switching of the configuration on varying the pH values.

On the $SrMnO_3$ 001 surface (Fig. 2(a)), at pH = 1, the dissolution of the surface Mn atoms up to the 25% surface vacancy formation is found to be most suitable up to oxidative potentials of 1.6 V_{SHE}. Beyond this potential, the surface leaching of 66% surface atoms is more suitable. Shifting to neutral pH, the most stable surface configuration corresponds to 25% surface vacancy up to 1.8 V_{SHE}. The formation of 66% surface vacancy is more preferred beyond that potential range. The alkaline pH shows a greater stability of the pristine surface at low oxidative potential (around 1.5 V_{SHE}), beyond that, the 25% vacancy formation shows more feasibility.

A differing stability trend is observed for the $SrFeO_3$ surface (Fig. 2(b)). The most stable surface configuration corresponds to the leaching of the surface Fe atoms to 25% at the potential range up to 1.6 V_{SHE} at pH = 1. The stability of the pristine surface increases in the neutral and alkaline regions at low oxidative potentials. The relative stability of the surfaces with 50% surface vacancy shows a greater preference with the gradual increase in the potential. However, the potential window defining the corresponding stability region for these vacancy formations considerably varies. At pH 7, the pristine surface shows the highest stability up to 1.4 V_{SHE}, whereas at pH 14, the pristine surface shows the highest stability up to 1.7 V_{SHE}. Beyond that, the 50% vacancy formation is more preferable at both pH values.

$SrCoO_3$ and $SrNiO_3$ show a similar stability ordering of the surfaces (Fig. 2(c) and (d), respectively). At pH 1, the pristine surface shows the highest stability at a lower potential range (up to 1.6 and 1.7 V_{SHE} for $SrCoO_3$ and $SrNiO_3$, respectively). An increase in the potential up to 2 V_{SHE}, the surface with 25%

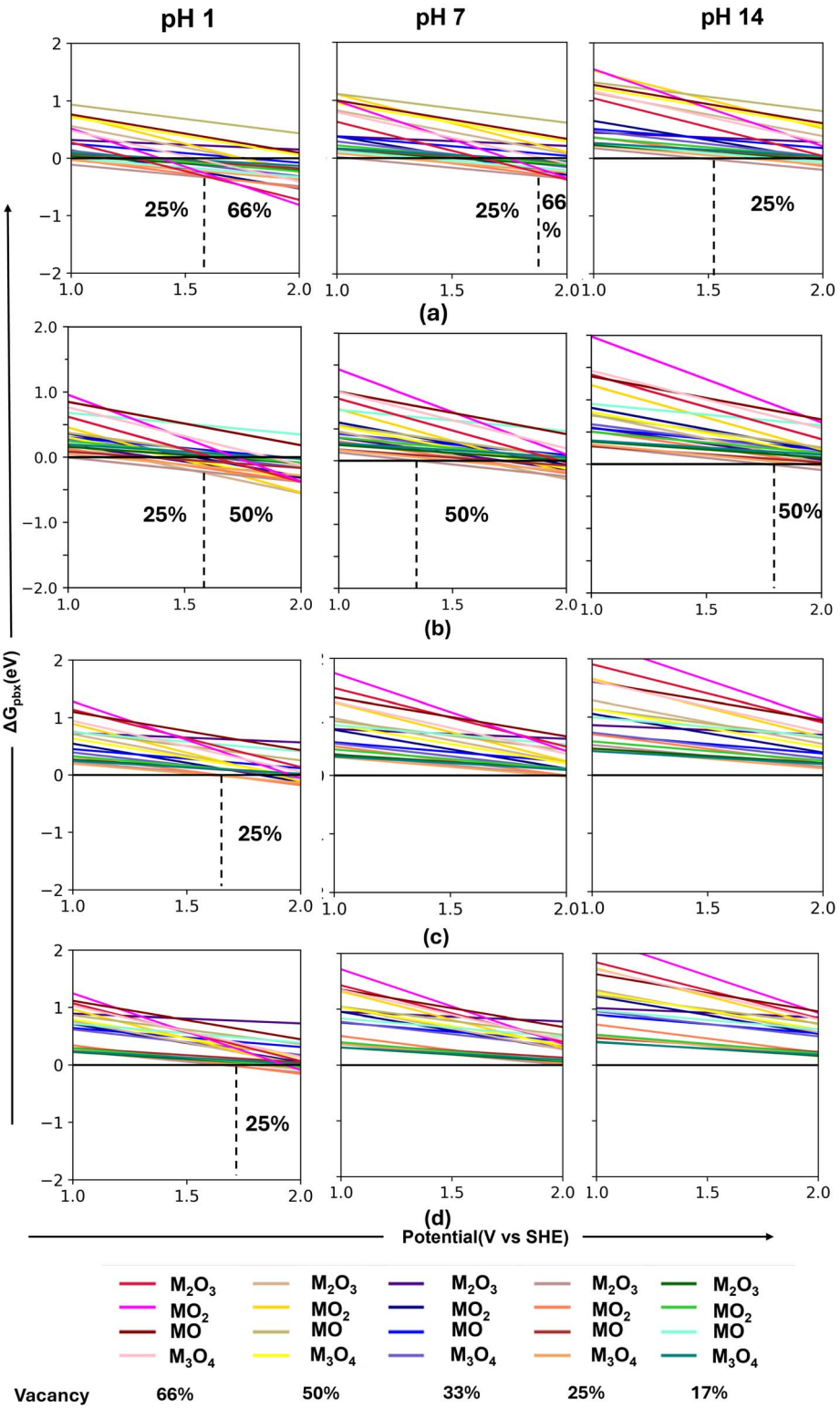

Fig. 2 (a)–(d) Illustrate the Pourbaix diagrams for $SrMnO_3$, $SrFeO_3$, $SrCoO_3$, and $SrNiO_3$, respectively, evaluated at pH 1, 7 and 14 under an applied potential range from 1.0 to 2.0 V. These diagrams include various corresponding metal oxides such as MO, MO_2, M_2O_3, and M_3O_4, and consider different metal vacancy compositions of 17%, 25%, 33%, 50% and 66%. Across all compositions and materials, the Pourbaix plots consistently denote enhanced thermodynamic stability associated with a 66%, 25% metal-site vacancy for $SrMnO_3$, 25% and 50% metal-site vacancy for $SrFeO_3$, 25%, and pristine surfaces for $SrCoO_3$ and $SrNiO_3$. The inset below shows the colour scheme considered to denote the different dissolution products.

vacancy becomes the most stable surface configuration. At pH 7 and 14, we found that the pristine surface has the most negative ΔG_{pbx} for all potential ranges, corresponding to the most stable structural configuration for both $SrCoO_3$ and $SrNiO_3$.

Next, we study the effect of doping with the different transition metal atoms on these four perovskite surfaces. We have considered 25% surface doping and calculated the electrochemical stability of the doped surfaces. Mn surface positions in $SrMnO_3$ have been doped with Fe, Co, and Ni atoms. For $SrFeO_3$, the doped surfaces have been created by doping the surface Fe atom with Mn, Co, and Ni. On the other hand, Co and Ni atoms on $SrCoO_3$ and $SrNiO_3$ surfaces, respectively, are doped with Mn, Fe, and Ni dopants, and Mn, Fe, and Co dopants. The doped surfaces are denoted as $M^*(M)$. Here, M^* corresponds to the dopant metal, and M denotes the host metal. For example, Fe-doped $SrMnO_3$ surface will be denoted as Fe(Mn).

$$SrM^*_nM_{1-n}O_3 + zyH_2O \rightarrow SrM^*_nM_{1-n-y}O_3 + yMO_z + 2zyH^+ + 2zye^- \quad (2)$$

$$SrM^*_nM_{1-n}O_3 + zyH_2O \rightarrow SrM^*_{n-y}M_{1-n}O_3 + yM^*O_z + 2zyH^+ + 2zye^- \quad (3)$$

$$SrM^*_nM_{1-n}O_3 + z(y1+y2)H_2O \rightarrow SrM^*_{n-y1}M_{1-n-y2}O_3 + y1M^*O_z + y2MO_z + 2z(y1+y2)H^+ + 2z(y1+y2)e^- \quad (4)$$

Fig. 3 shows the two-dimensional stability plots of the doped perovskite surfaces. The Pourbaix energies are calculated considering the most stable surface configuration detected for each surface. In the presence of the surface dopants, the dissolution of the surface metal ions could follow three different pathways depending upon the type of metal leaching (eqn (2)–(4)). The formation of metal oxides from both the host (M) and dopant (M^*) metal atoms of the surface could lead to the generation of surface vacancies. On the other hand, either the host or the dopant metal atom could leach out and form a single phase of the metal oxide. Further details for the computations are provided in Section S-II in the SI.

On doping the different transition metal dopants, both $SrMnO_3$ and $SrFeO_3$, show considerable negative free energies for the creation of the surface vacancies. Both these surfaces will lead to the dissolution of the surface metal atoms. For $SrFeO_3$, we find a narrow stability region. For Mn- and Co-doped $SrFeO_3$, the stability region corresponds to a pH value varying between 4.5 and 14, and the potential range between 1 and 1.4 V_{SHE}. With Ni as the surface dopant, the stability region corresponds to 3.9 to 14 pH and potential 1 to 1.6 V_{SHE}. On the other hand, $SrNiO_3$ and $SrCoO_3$ show a considerable range of stable regions. At acidic pH, the stable region corresponds to lower oxidative potentials. However, at neutral and alkaline pH, the stability region corresponds to both lower and higher oxidative potentials.

To understand the differing stability trend, we analyze the electronic d-band centers of the surface host metals (Fig. 4(a)). For the undoped surfaces, a shift in the d-band center to more negative energies is observed on moving from $SrMnO_3$ to $SrFeO_3$ to $SrCoO_3$ to $SrNiO_3$. The shaded bars show the d-band center values of the surfaces without the dopant in Fig. 4a. The d-band center for the Mn in $SrMnO_3$ is −0.59 eV from the Fermi energy, whereas the corresponding values are −1.66 eV for $SrFeO_3$, −1.75 eV for $SrCoO_3$, and −2.07 eV for $SrNiO_3$. A shift in the d-band centers to more negative energies implies lower reactivity of the surfaces with the electrolyte and aqueous molecules. This results in an increasing electrochemical stability of the pristine surfaces across a wide range of pH and potential values of the undoped surfaces from $SrMno_3$ to $SrFeO_3$ to $SrCoO_3$ to $SrNiO_3$ (Fig. 2a–(d)).

To further elucidate the effect of d-band center positioning with respect to the Fermi level in governing surface stability, we compare the d-band center values with the free energies associated with the formation of 25% surface vacancies on the pristine surfaces. The tendency for surface vacancy formation varies significantly depending on the surface structure, solution pH, and applied electrochemical potential. The direct comparison of individual key dissolution steps across different surfaces is challenging. Nevertheless, our analysis shows that the formation of 25% surface vacancies is thermodynamically feasible for all the surfaces considered. Therefore, we compare the dissolution free energies associated with the formation of 25% surface vacancies with the corresponding d-band center positions. Fig. 4(b) presents this comparative analysis. The resulting linear correlation indicates that as the d-band center shifts to more negative energies, the dissolution process becomes increasingly endothermic. This trend demonstrates that the position of the d-band center plays a crucial role in determining surface stability. Specifically, a less negative d-band center strengthens interactions with solvent molecules, thereby promoting surface dissolution.

A comparison of the average d-band centers of the host metal centers on the doped surfaces (Fig. 4a) shows great similarity to the undoped surfaces. For $SrMnO_3$, the d-band center values vary within the range −0.54 to −0.81 eV. The doping with Co slightly reduces the d-band center values to the more negative side (−0.81 eV). With $SrFeO_3$, the d-band center values marginally vary in the presence of the different dopants. The values correspond to −1.60 for Mn(Fe), −1.58 eV for Co(Fe), and −1.49 eV for Ni(Fe). Both the $SrCoO_3$ and $SrNiO_3$ doped surfaces show the highest negative values for the d-band centers. The corresponding values vary within the range −1.89 to −2.22 eV for $SrCoO_3$, and −1.90 eV to −2.18 eV for $SrNiO_3$. In the case of $SrCoO_3$, the d-band center values for the doped surfaces are slightly more negative than the undoped surfaces, with the highest negative value (−2.22 eV) obtained for Mn(Co). On the other hand, for $SrNiO_3$, the d-band center value for Mn(Ni) is only greater than the undoped surface. For both Fe(Ni) and Co(Ni), the d-band center value becomes less negative (−1.93 eV and −1.90 eV, respectively) compared to the undoped surface.

The d-band center of the B-site metal ions has been known to modulate the catalytic activity and choice of the particular reaction pathway. In this study, we find that the relative stability of the perovskite surfaces could also be governed by the alignment of the d-band center relative to the Fermi energy level. A strong

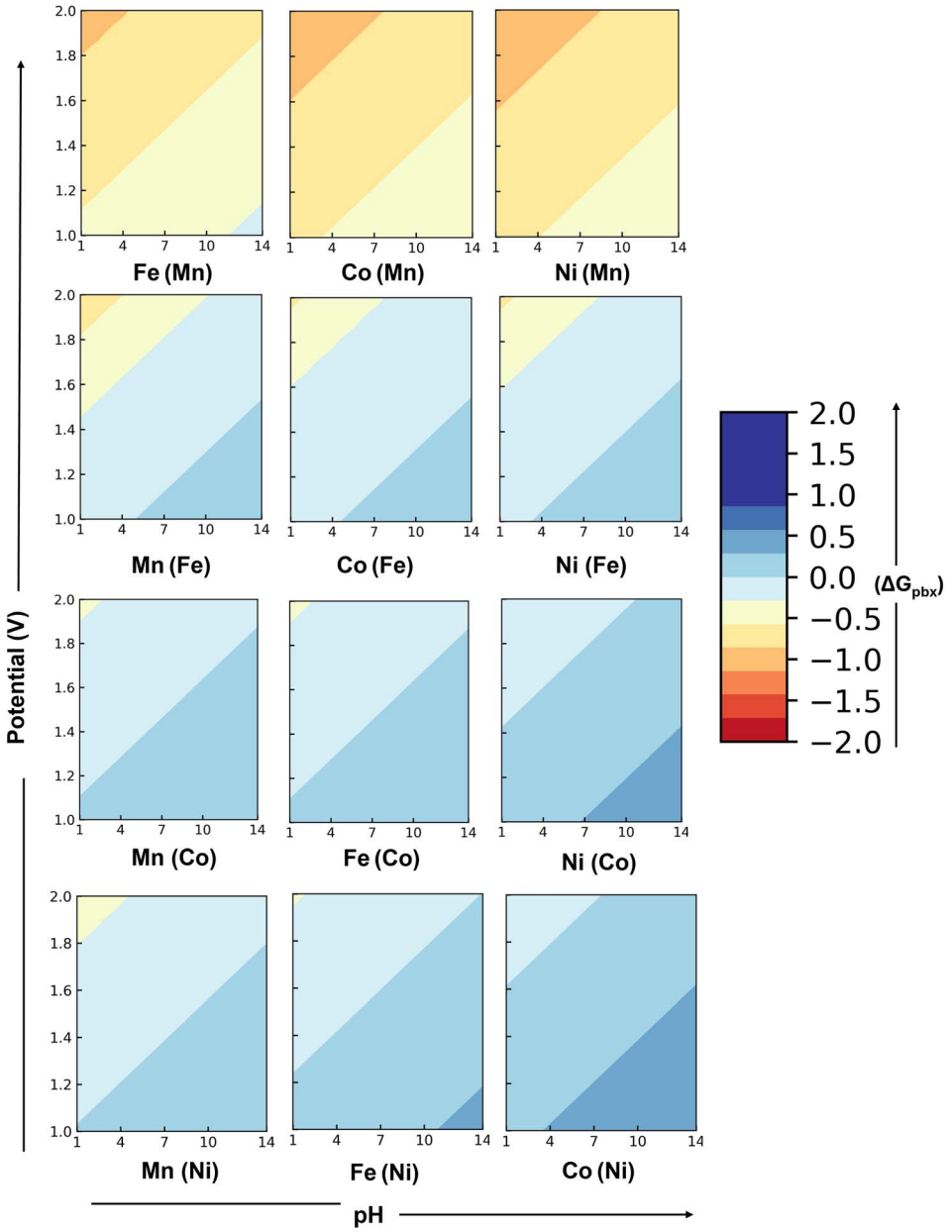

Fig. 3 The Pourbaix plot with pH on the *x*-axis and potential on the *y*-axis. The right-hand scale corresponds to the evaluation of ΔG_{pbx}. The blue region indicates thermodynamic stability, while the yellow and red regions denote instability. From the plot, it is evident that only $SrCoO_3$ and $SrNiO_3$ exhibit a wide stable region, while $SrFeO_3$ shows a comparatively narrow stable domain. Doped surfaces are denoted as $M^*(M)$, where M^* represents the dopant element, and M denotes the host B-site cation of the perovskite surface. Accordingly, Fe(Mn), Co(Mn), and Ni(Mn) correspond to Fe-, Co-, and Ni-doped $SrMnO_3$ surfaces, respectively. A similar nomenclature is adopted for the remaining doped surfaces.

correlation between surface dissolution free energy values and the position of the d-band center has been obtained (Fig. 4b). Both $SrCoO_3$ and $SrNiO_3$ show good stability in both doped and undoped forms due to the deeper positioning of the d-band center with reference to the Fermi energy level.

Doping influences the catalytic activity of the perovskite surfaces

Having determined the electrochemical stability of the surfaces, we analyze the catalytic activity of the pristine and doped surfaces for OER. The stability and surface configurations of the surfaces will largely modulate the catalytic activity. On the perovskite oxide surfaces, among the different mechanisms, the adsorbate evolution mechanism (AEM) and lattice oxygen mechanism (LOM) compete during the oxidation of water to produce O_2.[13,32] Fig. 5a shows the two mechanisms. AEM (black pathway in Fig. 5a) involves the adsorption of the oxygenated intermediates at the surface metal sites. The evolution of O_2 occurs *via* the formation of the different intermediates OH*, O*, and OOH*. In contrast, the LOM pathway (red pathway in Fig. 5a) enables lattice oxygen atoms to directly participate in

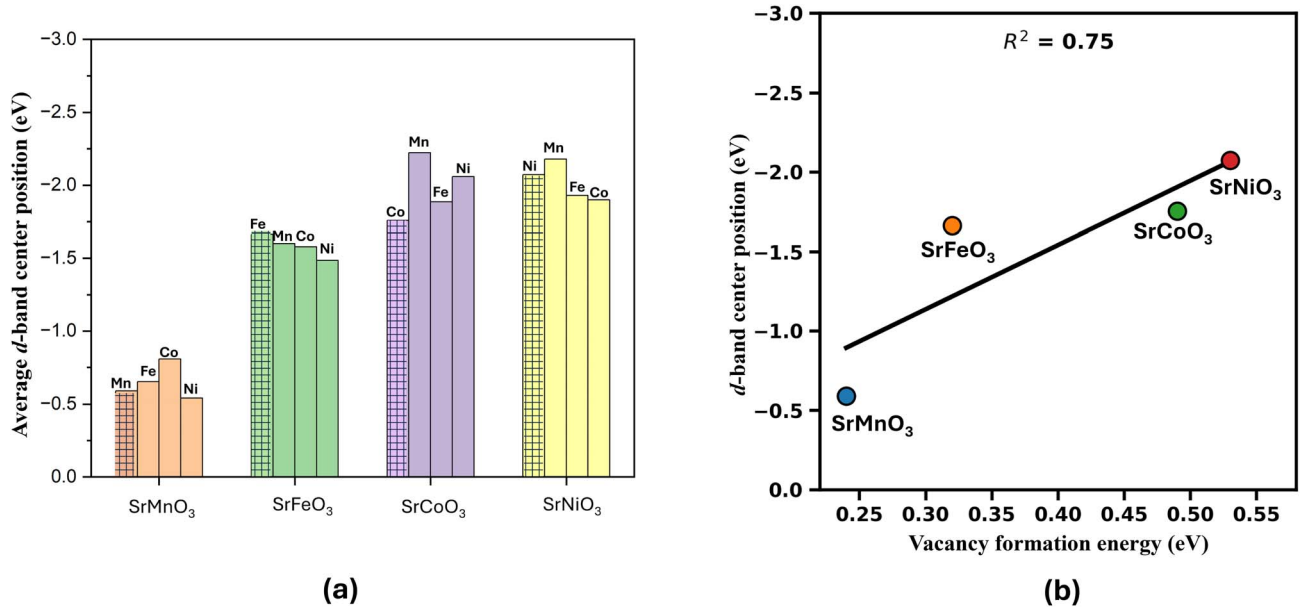

Fig. 4 (a) The electronic d-band centers in eV of surface host atoms in $SrMnO_3$, $SrFeO_3$, $SrCoO_3$, and $SrNiO_3$, respectively, (from left to right) without and with the different surface dopants. The *x*-axis represents the different materials, while the *y*-axis indicates the average d-band center. Shaded bars correspond to the d-band center values of the undoped surfaces. The d-band center values are given relative to the Fermi energy level. (b) The plot of free energy at 25% surface vacancy (along *x*-axis) on the pristine surfaces with the d-band center (*y* axis). A linear correlation is obtained with R^2 for the linear fit of 0.75.

O–O bond formation. The strength of the lattice O bond with the surface transition metal atoms determines the reaction thermodynamics and the overpotential to drive the oxidation reaction of H_2O to molecular O_2. The evolution of the O_2 creates a vacancy on the surface ($vacO_2$, Fig. 5a). In the next step, the adsorption of H_2O leads to the formation of adsorbed OH* at the vacancy site (vacOH* in Fig. 5a, red pathway). The removal of a proton and an electron from vacOH* regenerates the catalytic site in the fourth electrochemical step.

The reaction free energies of the key OER intermediates on the pristine surfaces of the four perovskite materials are computed to elucidate the relative ordering of catalytic activity and the preferred reaction pathways. The reaction free energy values are calculated using the computational hydrogen electrode method.[12] The computational details are provided in Section S-I in the SI. Fig. S1 presents the free-energy diagrams for the pristine surfaces along their most favorable reaction pathways, while Table ST1 summarizes the corresponding reaction free energies and overpotential values. $SrMnO_3$ and $SrFeO_3$ favor the AEM, with calculated overpotentials (η_{TD}) of 0.94 and 0.7 V, respectively.

On pristine $SrCoO_3$ and $SrNiO_3$ surface sites, the AEM is found to have higher η_{TD} compared to LOM. For LOM, the corresponding η_{TD} values are 0.51 and 1.06 V, respectively. On the other hand, for AEM, the η_{TD} values are 0.66 V and 1.16 V (Table ST6, SI), respectively. The formation of the OOH* intermediate shows the highest endothermicity on $SrCoO_3$ and corresponds to the PDS for the AEM pathway. On the $SrNiO_3$ surface, the second step, formation of O* intermediate, corresponds to the PDS.

The selectivity of the mechanistic pathways for OER on pristine $SrCoO_3$ and $SrNiO_3$ surfaces is in good agreement with previous studies.[13,16,87–89] The binding strength of the O* intermediate is the determining factor, responsible for the preferential selectivity of the LOM *vs.* AEM mechanism. To understand the preferences in the mechanistic pathway, we analyse the metal–O bond strength of the O* intermediate and plot the crystal orbital Hamilton population (COHP) density in the bonding and antibonding metal–O bands.[90] Fig. 5b and c show the COHP plots for the O* intermediates on $SrCoO_3$ and $SrNiO_3$. For $SrMnO_3$ and $SrFeO_3$ surfaces, the corresponding COHP plots are given in Fig. S3 in the SI. The vertical line in black differentiates the bonding and antibonding energy states; on the left-hand side of each plot, the antibonding energy states are shown, whereas the bonding energy states are on the right-hand side of the vertical line. The black horizontal line denotes the Fermi energy.

Analysing the COHP plots, we find that for the O* intermediate on both $SrCoO_3$ and $SrNiO_3$ surfaces, the antibonding metal–O* bands are filled up compared to $SrMnO_3$ and $SrFeO_3$ surfaces. This results in a slight elongation of the metal–O* bond, thereby enhancing the possibility of bonding with the lattice O atoms. The occupancy of the antibonding bands destabilizes the O* intermediate in comparison to the $vacO_2^*$, resulting in the preference for LOM (Fig. S3 in the SI). The corresponding antibonding states are less occupied for $SrMnO_3$, and $SrFeO_3$ surfaces, and the integrated crystal orbital Hamilton population (ICOHP) values in Fig. S3 (SI) are greater than the values shown in Fig. 5(b) and (c). This indicates greater

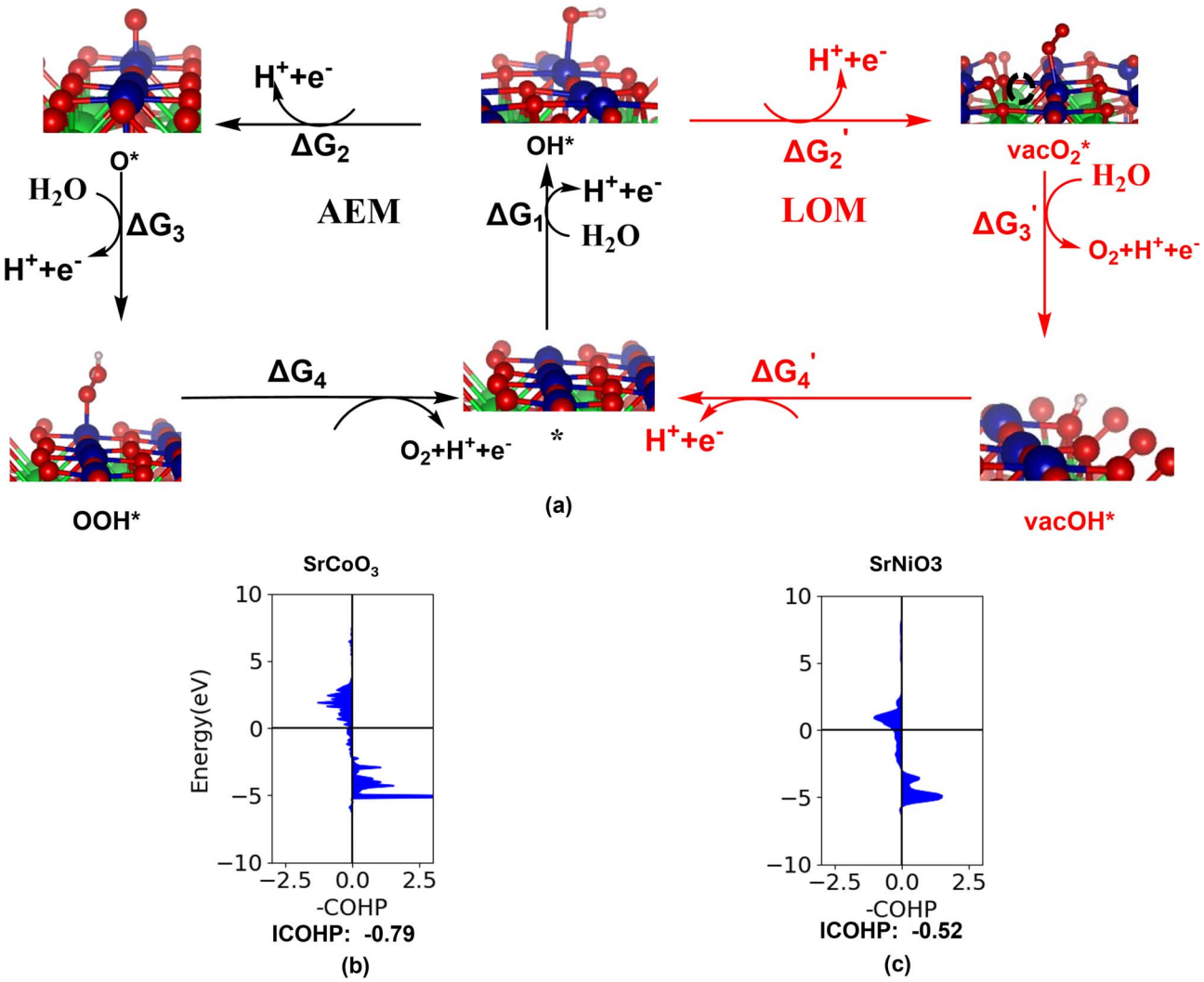

Fig. 5 (a) The adsorbate evolution mechanism (AEM) and the lattice oxygen mechanism (LOM) are shown. The black pathway represents the AEM route, while the red pathway corresponds to the LOM route. The proton-coupled-electron transfer is shown in each step, and the free energy changes are denoted as ΔG_i values. (b)–(c) The lower panel presents the crystal orbital Hamilton population (COHP) plots and the corresponding integrated crystal orbital Hamilton population (ICOHP) values for metal–O* bond on undoped $SrCoO_3$ and $SrNiO_3$ (001) surfaces, respectively. The black vertical line distinguishes bonding from antibonding states; the energy levels on the left of this line correspond to antibonding states, while those on the right represent bonding states. The black horizontal line indicates the Fermi energy.

metal–O* bond strength on $SrMnO_3$ and $SrFeO_3$ 001 surfaces and preference for AEM over LOM.[13]

The relative trend in the catalytic activity of the pristine surfaces shows good coherence with previous experimental and theoretical reports.[13,16,87–89] Comparing the catalytic activity of $SrMnO_3$, $SrFeO_3$, $SrCoO_3$, and $SrNiO_3$ (Table ST1 in SI), we find that the pristine $SrCoO_3$ surface is most active for OER.

Since $SrCoO_3$ and $SrNiO_3$ show the highest stability, in the proceeding discussion, we will only consider these surfaces with and without the surface dopants to study the electrocatalytic activity. The reaction free energy values for the AEM and LOM pathways on the doped surfaces for $SrCoO_3$ and $SrNiO_3$ are shown in Table 1. For comparison, we have given the corresponding values for the undoped surfaces of $SrCoO_3$ and $SrNiO_3$. The potential determining steps (PDS) are denoted in bold, and overpotential (η_{TD}) values are in column 8 in Table 1. For each surface, the catalytic site with the lowest η_{TD} values is given in Table 1. We denote the active surface sites using the nomenclature M_{1M_2}(Co) and M_{1M_2}(Ni), where M_1 corresponds to the dopant, and M_2 denotes the active site among the dopant or the host. Within the parentheses, we write the host metal atom. The Co_{Co}(Co) and Ni_{Ni}(Ni) for $SrCoO_3$ and $SrNiO_3$ denotes the undoped surfaces. The reaction free energies for the other sites with higher η_{TD} values are given in Table ST6 in the SI.

When considering the LOM pathway, we analyse oxygen vacancy formation at all unique oxygen sites surrounding both the host and dopant metal atoms. For the dopant, we identify a single unique oxygen site bridging the host and dopant metal centers. On the otherhand, two distinct lattice oxygen sites associated with the host metal participate in vacancy formation: the oxygen bridging two host metal atoms and the oxygen bridging the host and dopant metal centers (Fig. S2, SI). We

Table 1 Reaction free energies (ΔG) along the preferred OER pathway (AEM/LOM) for the undoped and the doped $SrCoO_3$ and $SrNiO_3$ perovskite surfaces. The active sites are shown in Column 2. The ΔG values are shown in Columns 3–6. The potential-determining step (largest ΔG) is highlighted in bold. Column 7 shows the G_{max} values and the corresponding reaction step as RDS. The corresponding η_{TD} values and preferred mechanism are denoted in columns 8 and 9, respectively

Material	$Dopant_{Active\ site}(host)$	ΔG_1	$\Delta G_2/\Delta G_2^{'}$	$\Delta G_3/\Delta G_3^{'}$	$\Delta G_4/\Delta G_4^{'}$	G_{max}	η_{TD}	Mechanism
$SrCoO_3$								
Undoped	$Co_{Co}(Co)$	**1.74**	0.71	1.15	1.33	$0.21(\Delta G_1)$	0.51	LOM
Mn-doped	$Mn_{Mn}(Co)$	**2.08**	0.94	1.04	0.86	$0.55(\Delta G_1)$	0.85	LOM
Fe-doped	$Fe_{Fe}(Co)$	1.25	**1.47**	1.30	0.90	$-0.06(\Delta G_2^{'})$	0.24	LOM
Ni-doped	$Ni_{Ni}(Co)$	1.36	0.54	**1.64**	1.39	$0.11(\Delta G_3^{'})$	0.41	LOM
$SrNiO_3$								
Undoped	$Ni_{Ni}(Ni)$	1.31	0.19	1.13	**2.29**	$0.76(\Delta G_4^{'})$	1.06	LOM
Mn-doped	$Mn_{Ni}(Ni)$	1.55	0.47	1.13	**1.57**	$0.76(\Delta G_1)$	0.34	LOM
Fe-doped	$Fe_{Fe}(Ni)$	1.74	1.62	**1.77**	−0.21	$0.54(\Delta G_1 + \Delta G_2 + \Delta G_3)$	0.54	AEM
Co-doped	$Co_{Co}(Ni)$	**1.84**	1.55	1.79	−0.25	$0.59(\Delta G_1 + \Delta G_2 + \Delta G_3)$	0.61	AEM

have considered all these lattice O to evaluate the minimum energy pathways. In Table ST6 (SI), reactions at the host metal site are distinguished based on the participating lattice oxygen, denoted as $[O_H]$ and $[O_D]$ in column 2. $[O_H]$ corresponds to the oxygen bridging two host metal atoms, whereas $[O_D]$ corresponds to the oxygen bridging the host and dopant metal atoms.

A considerable reduction in the η_{TD} values has been observed with the surface doping. On $SrCoO_3$ surfaces, we find that for all the doped surfaces, the active site with the lowest η_{TD} values corresponds to the doped sites. LOM shows a slightly greater preference compared to the AEM with all the surface dopants. The $\Delta G_2^{'}$ corresponding to the formation of the $vacO_2^*$ intermediate has a lower thermodynamic barrier compared to O* formation. This favors the LOM pathway.

The PDS shows a wide variation depending on the active sites and the surface dopants. The $Mn_{Mn}(Co)$ show the formation of OH* as having the highest endothermicity. For $Fe_{Fe}(Co)$, the formation of $vacO_2^*$ (step 3 for LOM, Fig. 5a) is the PDS, whereas the $Ni_{Ni}(Co)$ site shows the highest endothermicity for the formation of the vacOH* intermediate.

The $SrNiO_3$ surface with the different surface dopants shows a differing trend. Unlike the Ni_{Ni} site (undoped surface), the AEM is found to be the most preferred pathway with Fe and Co surface doping ($Fe_{Fe}(Ni)$ and $Co_{Co}(Ni)$). Though $vacO_2^*$ formation shows more preference than O* formation, on these sites, the regeneration of the catalytic site (the fourth step, ΔG^*) has been found with high endothermicity while following the LOM.

Compared to the undoped surface ($Ni_{Ni}(Ni)$), both $Fe_{Fe}(Ni)$ and $Co_{Co}(Ni)$ sites show an increment in the catalytic activity. The PDS for $Fe_{Fe}(Ni)$ corresponds to the formation of the vacOH* intermediate with η_{TD} value of 0.54 V. In contrast, on the $Co_{Co}(Ni)$ site, the PDS corresponds to the formation of the OH* intermediate. The corresponding η_{TD} value is 0.61 V. With Mn-doping, we have seen the highest catalytic activity. On both $Mn_{Ni}(Ni)$ and $Mn_{Mn}(Ni)$ sites, the η_{TD} values are considerably lower than the Ni_{Ni} site (Table 1 and ST6 in the SI). Both sites show higher preference for LOM. The most active site is Mn_{Ni} (Ni), with a PDS corresponding to $\Delta G_4^{'}$ (η_{TD} value of 0.34 V).

Surface oxygen vacancy formation is often associated with significant structural distortion and, in some cases, surface collapse of perovskite oxides. Previous studies have shown that lattice oxygen participation in the oxygen evolution reaction, accompanied by the formation of oxygen vacancies, can accelerate surface degradation and metal dissolution.[91–94]

In the present study, however, we do not observe such structural instability for either $SrCoO_3$ or $SrNiO_3$ (with or without surface dopants) upon surface O-vacancy formation. Fully relaxed surface geometries exhibit only minimal distortions following lattice oxygen participation in O_2 evolution (Fig. S7 in SI). These results indicate that both $SrCoO_3$ and $SrNiO_3$ surfaces maintain structural stability under the considered reaction conditions.

Fig. 6(a) and (b) show the comparison of the reaction free energies on the doped surfaces with the undoped surfaces. The ideal catalysts, with ΔG values of 1.23 eV for each step, are also plotted in these diagrams (black lines). Compared to the undoped surfaces, a considerable reduction in the ΔG value of the PDS is observed for the most active doped surfaces.

The difference between the center of the d-band and p-band has been known to influence the preference of the mechanism in the OER.[32,52,53,95–97] The decrease in the gap between the d-band and p-band center promotes the increase in the covalency of the M–O bond and could enhance the preference for LOM. In this study, we analyze the d-band centers of the host (M_{nd}) and dopant (D_{nd}) B-site ions and determine the difference with the O p-band centers of the different types of lattice O available in the surroundings of these metal ions. Fig. S6 shows the different O types present surrounding the dopant and the host metal center, and Table ST7 in the SI gives the differences in the band centers. For most of the cases, the differences in the d-band and p-band centers are minimal except for $SrCoO_3$ with the Mn dopant. We have obtained that formation of $vacO_2^*$ is more favorable than that of the O* intermediate, corresponding to favoring the lattice O participating in the reaction. However, in most of the cases, $vacO_2^*$ formation does not correspond to the potential determining step (PDS). Therefore, the specificity

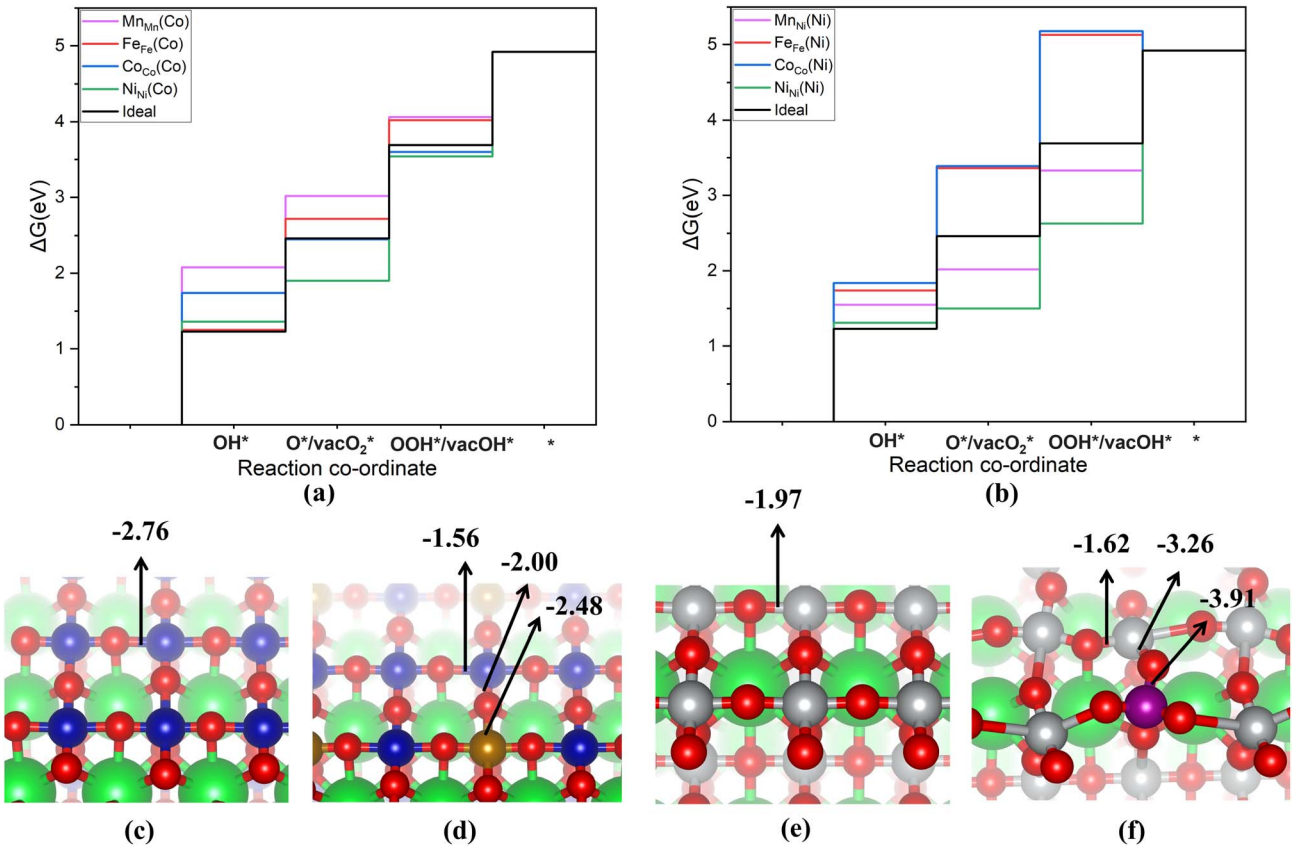

Fig. 6 (a) and (b) Free energy diagrams (FEDs) for the most favorable reaction pathways on various doped perovskite surfaces of $SrCoO_3$ and $SrNiO_3$. The black lines represent an ideal catalyst surface, with each reaction step assigned an energy of 1.23 eV. The FEDs in purple, red, blue, and green correspond to Mn-, Fe-, Co-, and Ni-doped surfaces, respectively. (a) shows the FEDs for $SrCoO_3$ with different dopants, and (b) shows those for $SrNiO_3$ with different dopants. (c) and (d) The ICOHP values for undoped $SrCoO_3$ and Fe-doped $SrCoO_3$, respectively. (e) and (f) Show the ICOHP values for undoped $SrNiO_3$ and Mn-doped $SrNiO_3$.

towards the preference of the mechanism is not solely dependent on the $\Delta G_{vacO_2^*}$ values.

To understand the differing trends in the reactivity of the doped surfaces, we analyze the electronic structure of the surfaces. For $SrCoO_3$, Mn-doping leads to stabilizing the d-bands of the active site to the most negative values (−2.22 eV). This results in the lowest catalytic activity and the highest η_{TD} values compared to the undoped surface. With the Fe doping to $SrCoO_3$ surface, the catalytic activity is enhanced the most. The Fe site exhibits the least negative value for the d-band center (−1.46 eV), resulting in the greatest reduction in the endothermicity of the OH* intermediate. This is the possible reason for enhancing the catalytic activity of this site. The Fe_{Co}(Co) site, though, has an almost similar d-band center as the undoped surface (−1.88 eV and −1.76 eV for Fe_{Co}(Co) and Co_{Co}, respectively); nevertheless, an increase in the activity is observed. We find considerable surface structure distortion on Fe doping (Fig. 6d). An increase in the binding strength of Fe with lattice O is observed. The Co–$O_{lattice}$ has been elongated compared to the undoped surface. We have calculated the ICOHP values to determine the metal–$O_{lattice}$ bond strength, as shown in Fig. 6(d) and compared to the undoped surface (Fig. 6c). The corresponding ICOHP values are lower than those of the undoped surface, reflecting the lowering of the bond strength. The structural distortions allow the creation of dangling valences on the surface metal sites and increase its activity for OER. An almost similar activity is obtained for the Co_{Fe}(Co) and Fe_{Fe}(Co) sites. For the other doped surfaces, we have not observed a significant deviation of the ICOHP values in comparison to the undoped surfaces. Table ST8 in the SI shows these ICOHP values.

Similar structural distortions and alignment of the d-band centers of the $SrNiO_3$ surface, on doping with the different transition metals, have been found to tune the catalytic activity. While following the LOM mechanism, we find that the vacOH* intermediate shows extensive stability on both the undoped and doped surfaces, except for Mn_{Ni}(Ni) and Mn_{Mn}(Ni) sites. This increases the endothermicity of $\Delta G_4^{'}$ (corresponding to catalytic site regeneration), leading to an enhancement of the η_{TD} value. Therefore, to enhance the activity of these sites, it is important to reduce the binding affinity of the H to the lattice O site. Therefore, the lattice O–metal bonds need to be strengthened to reduce the endothermicity of the fourth step. Stronger binding of lattice O to the metal atoms will reduce the O–H bond strength in vacOH* and hence the endothermicity of $\Delta G_4^{'}$.

The ICOHP values of the lattice O with the metal centers increase on doping with Fe, Co, and Mn in comparison to the undoped $SrNiO_3$ surface. A maximum increment in the binding strength of the lattice O is observed for the Mn-doped surface. Therefore, for Mn_{Ni}(Ni) and Mn_{Mn}(Ni) sites, formation of vacOH* shows higher endothermicity than other doped surfaces. A decrease in binding strength has been observed, providing an advantage for these sites. The thermodynamic barrier of the fourth step ($\Delta G_4'$) is reduced, thereby the η_{TD} values have been reduced to a great extent for Mn_{Ni}(Ni) and Mn_{Mn}(Ni) sites. Fig. 6(f) shows the corresponding ICOHP values for lattice O bonded to Mn_{Ni}(Ni) and Mn_{Mn}(Ni) sites. For the other surfaces (doped and undoped $SrNiO_3$ surfaces), the ICOHP values are shown in Table ST8 in the SI.

To understand the effect of dopant concentration on the OER activity, we perform a systematic activity analysis of the most active doped surface: Fe-doped $SrCoO_3$ surfaces with Fe concentrations of 17%, 25%, 33%, and 50%. The 25% doping level is achieved by substituting one surface Co atom in a 2×2 (001) surface supercell of $SrCoO_3$. The other doping concentrations 17%, 33%, and 50% are obtained by substituting one, two, and three surface Co atoms, respectively, in a 2×3 surface supercell of $SrCoO_3$.

We have considered both the host and dopant atoms as potential active sites and compared the AEM and LOM pathways across different dopant concentrations. Fig. 7 shows a comparison of the theoretical η_{TD} values as a function of Fe doping percentage. In all cases, the LOM pathway exhibits lower η_{TD} values than AEM. At a Fe doping concentration of 17%, the Fe_{Co}(Co) site exhibits the lowest η_{TD}. However, as the dopant concentration increases, the Fe_{Fe}(Co) site becomes the most favorable active site for OER. Among all doping percentages studied, the 25% Fe-doped surface shows the lowest η_{TD} values for both Fe_{Co}(Co) and Fe_{Fe}(Co) sites. Although the difference in the corresponding η_{TD} values is minimal at the 25% surface doping, the Fe_{Fe}(Co) site is slightly more favorable.

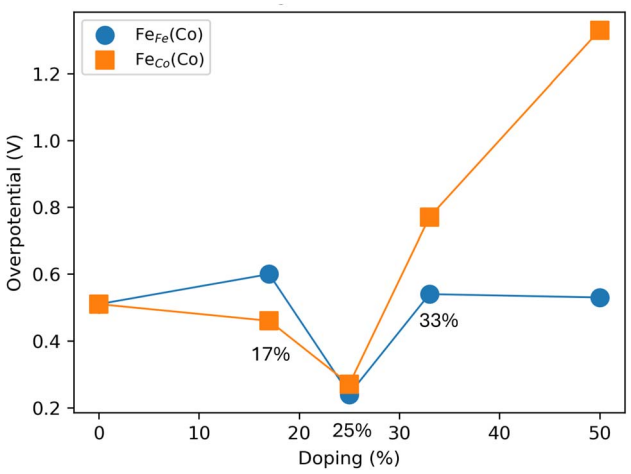

Fig. 7 The OER activity analysis of the effect of surface Fe concentration on 001 $SrCoO_3$ surfaces. The considered surface doping concentrations are 17%, 25%, 33%, and 50%. 0% corresponds to the undoped $SrCoO_3$ surface. The Fe_{Fe}(Co) site is denoted in blue circular markers, whereas for the Fe_{Co}(Co) site, orange square markers are used. A maximum activity is observed for the 25% surface doping.

Recent studies have shown that B-site doping of perovskite surfaces can effectively modulate the positions of the O-p band and metal d-band centers. By varying the Mn doping concentration on the $SrCoO_3$ surface, the electronic structure can be systematically tuned for different applications.[98] More prominently, Fe doping of $SrCoO_3$ surfaces has been reported to significantly enhance the O_2 evolution reaction (OER) activity.[99] Several Sr–Fe–Co–O perovskite compositions have been synthesized by varying the Fe/Co ratio. $Sr_2Co_{1.5}Fe_{0.5}O_{6-\delta}$ exhibits the highest OER performance, with an overpotential of 318 mV at 10 mA cm^{-2} and a Tafel slope of 44.8 mV dec^{-1}.[99] These experimental findings are in good agreement with our computational results. In particular, we find that maintaining the Fe dopant concentration at approximately 25% yields the maximum O_2 evolution activity on the Fe-doped $SrCoO_3$ surface (Fig. 7). Among the different active sites, Fe_{Fe}(Co) shows the highest activity. Although doping of the other perovskite surfaces has not yet been reported for OER application, our results demonstrate that tuning the dopant concentration on $SrNiO_3$ and $SrFeO_3$ surfaces can significantly enhance their catalytic activity for the oxygen evolution reaction.

The kinetics of the elementary electrochemical steps are important in defining catalytic activity. η_{TD} is evaluated at zero applied potential and corresponds to the elementary step with the largest thermodynamic free energy. However, in multistep electrochemical pathways, this step is not always the rate-determining step (RDS), particularly in cases where the potential-determining step (PDS) differs from the RDS.[100]

To address this, Exner and co-workers introduced a potential-dependent reactivity descriptor, $G_{max}(\eta)$, which directly identifies the RDS under an applied potential.[100] The descriptor is derived from the free energy changes of the elementary steps (ΔG_i, $i = 1, 2, 3, 4$) under an applied overpotential. Unlike η_{TD}, $G_{max}(\eta)$ scales linearly with the free energy of the RDS, providing a more accurate reflection of catalytic activity.[101–103]

For OER catalysts, values of $G_{max}(\eta)$ less than or equal to 1.0 eV at $\eta = 0.3$ V are typically associated with good catalytic performance.[101] Accordingly, we have used this criterion in our analysis (Table 1) to identify the RDS and evaluate the efficiency of various active sites with different dopants. The specific ΔG_i values that govern the RDS are given in column 7.

The trend in G_{max} values indicates that, for the majority of active sites obtained in our study, the RDS is governed by a single elementary step. However, the corresponding step determining the RDS shows wide variation depending upon the active sites. The Co_{Co}(Co), Mn_{Mn}(Co) sites show ΔG_1 as the RDS. On the other hand, $\Delta G_2'$, $\Delta G_3'$, and $\Delta G_4'$ are found to be the RDS for Fe_{Fe}(Co), Ni_{Ni}(Co) and Ni_{Ni}(Ni) respectively. This suggests that the reaction kinetics in these sites are largely dictated by the energetics of the specific step with the largest G_{max} values.

In contrast, a different pattern emerges for certain dopants, most notably Fe and Co doped to the $SrNiO_3$ surfaces, where G_{max} is not confined to a single ΔG_i value. These surfaces instead show the cumulative contribution of multiple steps (*e.g.*, $\Delta G_1 + \Delta G_2 + \Delta G_3$). The kinetic limitation is distributed over

several transitions rather than a localized single barrier on these surface sites. The multistep character in defining the RDS reflects a more complex kinetic landscape, where the reaction energetics of multiple intermediates determine the catalytic activity.

To assess the experimental viability of the doped surfaces, we have calculated the formation energies (E_{form}) for all perovskites with the different surface dopants using bulk metals as references for the dopants and the pristine surface as the reference for the host perovskite (Fig. S4 in the SI). In Section S-V in the SI, the details for the formation energy of the doped surfaces are shown.

A clear trend is observed in which the E_{form} becomes progressively less favorable when moving from early to late transition-metal dopants. While all dopants on $SrMnO_3$ surfaces show endothermic E_{form}, $SrFeO_3$ shows exothermic stabilization only for Mn doping. In contrast, most dopants with $SrCoO_3$ and $SrNiO_3$ surfaces exhibit exothermic formation energies, indicating enhanced thermodynamic stability. Notably, Fe-doped $SrCoO_3$ and Mn-doped $SrNiO_3$ surfaces, which exhibit good catalytic activity, display exothermic formation energies. Therefore, these compositions are experimentally viable.

Conclusions

In this study, we have analyzed the catalytic activity and reaction mechanism for OER on four perovskite oxide surfaces, namely $SrMnO_3$, $SrFeO_3$, $SrCoO_3$, and $SrNiO_3$. The electrochemical stability and catalytic activity for OER have been analyzed, focusing on the (001) surface termination of the pristine surface, and doped with different transition metal ions at the B-site. We have calculated the dissolution free energies across a wide pH range (acidic to alkaline) and oxidative potentials of 1–2 V *vs.* SHE to determine the electrochemical stability under these varying conditions. PDOS analysis of the (001) surfaces shows the O-p band center located 2.99–3.50 eV below E_{Fermi}, indicating that dissolution mainly proceeds through leaching of surface B-site transition metal ions.

Dissolution free energies (ΔG_{pbx}) are computed for surface vacancy creation of 17–66%. For $SrMnO_3$, Mn dissolution is most favorable (up to 66%) in acidic media, while neutral and alkaline pH favor only 25% or pristine surfaces depending on potential. $SrFeO_3$ surfaces are most stable with 50% vacancy formation at acidic pH, whereas pristine surfaces dominate stability at neutral and alkaline pH under low potentials. In $SrCoO_3$ and $SrNiO_3$, pristine surfaces are most stable at low potentials across pH 1–14. At higher oxidation potential and acidic pH, 25% vacancy formation is found to be possible. However, at neutral and alkaline pH, the pristine surfaces show extensive stability for the entire potential range.

With 25% surface doping of transition metals (Mn, Fe, Co, and Ni) wide variation in the electrocatalytic activity and stability is observed. Pourbaix free energy (ΔG_{pbx}) calculations of these doped systems reveal many dissolution pathways depending on whether the host, dopant, or both ions leach. $SrMnO_3$ do not show stability regions with any of the surface dopants. $SrFeO_3$ show a narrow stable region at the alkaline pH and low oxidative potential. However, $SrCoO_3$ and $SrNiO_3$ show stable regions at the neutral to alkaline pH. The positioning of the metal d-band centers with respect to the Fermi energy strongly influences the stability of the surfaces.

Next, we analyze the catalytic activity of pristine and doped $SrCoO_3$ and $SrNiO_3$ surfaces. OER is found to occur *via* two competing pathways: Adsorbate Evolution Mechanism (AEM) and the Lattice Oxygen Mechanism (LOM). The calculations show that undoped $SrCoO_3$ and $SrNiO_3$ favor LOM with η_{TD} values of 0.51 and 1.06 V, respectively. Analysis of COHP plots reveals progressive weakening of metal–O bonds from $SrCoO_3$ to $SrNiO_3$, promoting LOM. Surface doping further tunes catalytic activity: Fe-doping in $SrCoO_3$ reduces η_{TD} to as low as 0.24 V at the Fe_{Fe}(Co) site. In $SrNiO_3$, Mn-doping significantly lowers η_{TD} to 0.34 V at Mn_{Ni}(Ni) site. We found that surface distortion and the alignment of d-band center of the active sites considerably determine the relative activity of the surface sites. On varying the Fe-dopant percentages on $SrCoO_3$ surface, we find that 25% surface doping shows the highest catalytic activity for OER.

The activity descriptor $G_{max}(\eta)$ at the applied η of 0.3 V is used to analyse the rate-determining step (RDS). While most active sites exhibit a single step as the RDS, Fe- and Co-doped $SrNiO_3$ display a multistep process for determining the reaction rate. The design principle shown in this study to tune the catalytic activity and stability of perovskite oxide surfaces by surface doping will be of great importance for efficient catalyst development for OER.

Author contributions

S. S.: data curation, formal analysis, investigation, methodology, and visualization. N. K.: conceptualization, funding acquisition, methodology, project administration, resources, software, supervision, and visualization. Both authors contributed to writing the original draft, reviewing, and editing.

Conflicts of interest

The authors declare no conflicts of interest.

Data availability

The data related to computations will be available from the authors. Most of the data used to set up the figures has been provided in the manuscript and supplementary information (SI). Supplementary information is available. See DOI: https://doi.org/10.1039/d5ta07376f.

Acknowledgements

N. K. and S. S. acknowledge the Shiv Nadar Institution of Eminence and Shiv Nadar Foundation for financial assistance and computational support. The calculations are performed at the supercomputer (Magus).

Notes and references

1 Z. W. Seh, J. Kibsgaard, C. F. Dickens, I. Chorkendorff, J. K. Nørskov and T. F. Jaramillo, *Science*, 2017, **355**, eaad4998.
2 Y. Zhu, W. Zhou and Z. Shao, *Small*, 2017, **13**, 1603793.
3 L. Han, S. Dong and E. Wang, *Adv. Mater.*, 2016, **28**, 9266–9291.
4 B.-J. Kim, D. F. Abbott, X. Cheng, E. Fabbri, M. Nachtegaal, F. Bozza, I. E. Castelli, D. Lebedev, R. Schaublin, C. Copéret, *et al.*, *ACS Catal.*, 2017, **7**, 3245–3256.
5 R. S. Haszeldine, *Science*, 2009, **325**, 1647–1652.
6 N.-T. Suen, S.-F. Hung, Q. Quan, N. Zhang, Y.-J. Xu and H. M. Chen, *Chem. Soc. Rev.*, 2017, **46**, 337–365.
7 Y. Jin, H. Wang, J. Li, X. Yue, Y. Han, P. K. Shen and Y. Cui, *Adv. Mater.*, 2016, **28**, 3785–3790.
8 Y. Zheng, Y. Jiao, Y. Zhu, L. H. Li, Y. Han, Y. Chen, M. Jaroniec and S.-Z. Qiao, *J. Am. Chem. Soc.*, 2016, **138**, 16174–16181.
9 B. Han, M. Risch, Y.-L. Lee, C. Ling, H. Jia and Y. Shao-Horn, *Phys. Chem. Chem. Phys.*, 2015, **17**, 22576–22580.
10 O. Diaz-Morales, I. Ledezma-Yanez, M. T. Koper and F. Calle-Vallejo, *ACS Catal.*, 2015, **5**, 5380–5387.
11 W. Li, H. Tian, L. Ma, Y. Wang, X. Liu and X. Gao, *Mater. Adv.*, 2022, **3**, 5598–5644.
12 J. K. Nørskov, J. Rossmeisl, A. Logadottir, L. Lindqvist, J. R. Kitchin, T. Bligaard and H. Jonsson, *J. Phys. Chem. B*, 2004, **108**, 17886–17892.
13 J. S. Yoo, X. Rong, Y. Liu and A. M. Kolpak, *ACS Catal.*, 2018, **8**, 4628–4636.
14 H. Li, Y. Chen, J. Z. Y. Seow, C. Liu, A. C. Fisher, J. W. Ager and Z. J. Xu, *Small Sci.*, 2022, **2**, 2100048.
15 Y. Zhao, D. P. Adiyeri Saseendran, C. Huang, C. A. Triana, W. R. Marks, H. Chen, H. Zhao and G. R. Patzke, *Chem. Rev.*, 2023, **123**, 6257–6358.
16 I. C. Man, H.-Y. Su, F. Calle-Vallejo, H. A. Hansen, J. I. Martínez, N. G. Inoglu, J. Kitchin, T. F. Jaramillo, J. K. Nørskov and J. Rossmeisl, *ChemCatChem*, 2011, **3**, 1159–1165.
17 K. S. Exner, *Acc. Chem. Res.*, 2024, **57**, 1336–1345.
18 S. Singh and N. Karmodak, *ACS Appl. Energy Mater.*, 2024, **7**, 7854–7863.
19 M. Sokolov and K. S. Exner, *Chem Catal.*, 2024, **4**, year.
20 N. Karmodak and O. Andreussi, *ACS Energy Lett.*, 2020, **5**, 885–891.
21 N. Danilovic, R. Subbaraman, K.-C. Chang, S. H. Chang, Y. J. Kang, J. Snyder, A. P. Paulikas, D. Strmcnik, Y.-T. Kim, D. Myers, *et al.*, *J. Phys. Chem. Lett.*, 2014, **5**, 2474–2478.
22 J. Rossmeisl, A. Logadottir and J. K. Nørskov, *Chem. Phys.*, 2005, **319**, 178–184.
23 S. Cherevko, S. Geiger, O. Kasian, N. Kulyk, J.-P. Grote, A. Savan, B. R. Shrestha, S. Merzlikin, B. Breitbach, A. Ludwig, *et al.*, *Catal. Today*, 2016, **262**, 170–180.
24 Y. Zhu, W. Zhou, J. Yu, Y. Chen, M. Liu and Z. Shao, *Chem. Mater.*, 2016, **28**, 1691–1697.
25 G. K. K. Gunasooriya and J. K. Nørskov, *ACS Energy Lett.*, 2020, **5**, 3778–3787.
26 R. Frydendal, E. A. Paoli, B. P. Knudsen, B. Wickman, P. Malacrida, I. E. Stephens and I. Chorkendorff, *ChemElectroChem*, 2014, **1**, 2075–2081.
27 N. Hodnik, P. Jovanovic, A. Pavlisic, B. Jozinovic, M. Zorko, M. Bele, V. S. Selih, M. Sala, S. Hocevar and M. Gaberscek, *J. Phys. Chem. C*, 2015, **119**, 10140–10147.
28 K. S. Exner, *ChemElectroChem*, 2021, **8**, 46–48.
29 V. M, S. Singh, F. Bononi, O. Andreussi and N. Karmodak, *J. Chem. Phys.*, 2023, **159**, 111001.
30 D. A. Kuznetsov, B. Han, Y. Yu, R. R. Rao, J. Hwang, Y. Román-Leshkov and Y. Shao-Horn, *Joule*, 2018, **2**, 225–244.
31 N. Karmodak, L. Bursi and O. Andreussi, *J. Phys. Chem. Lett.*, 2021, **13**, 58–65.
32 A. Grimaud, O. Diaz-Morales, B. Han, W. T. Hong, Y.-L. Lee, L. Giordano, K. A. Stoerzinger, M. T. Koper and Y. Shao-Horn, *Nat. Chem.*, 2017, **9**, 457–465.
33 Z. Wang, Y.-R. Zheng, I. Chorkendorff and J. K. Nørskov, *ACS Energy Lett.*, 2020, **5**, 2905–2908.
34 J. Xu, C. Chen, Z. Han, Y. Yang, J. Li and Q. Deng, *Nanomaterials*, 2019, **9**, 1161.
35 M. De Graef and M. E. McHenry, *Structure of Materials: an Introduction to Crystallography, Diffraction and Symmetry*, Cambridge University Press, 2012.
36 J. Hwang, R. R. Rao, L. Giordano, Y. Katayama, Y. Yu and Y. Shao-Horn, *Science*, 2017, **358**, 751–756.
37 R. E. Cohen, *Nature*, 1992, **358**, 136–138.
38 K. Huang, R. S. Tichy and J. B. Goodenough, *J. Am. Ceram. Soc.*, 1998, **81**, 2565–2575.
39 J. Suntivich, H. A. Gasteiger, N. Yabuuchi, H. Nakanishi, J. B. Goodenough and Y. Shao-Horn, *Nat. Chem.*, 2011, **3**, 546–550.
40 E. Fabbri, M. Nachtegaal, T. Binninger, X. Cheng, B.-J. Kim, J. Durst, F. Bozza, T. Graule, R. Schäublin, L. Wiles, *et al.*, *Nat. Mater.*, 2017, **16**, 925–931.
41 B.-J. Kim, X. Cheng, D. F. Abbott, E. Fabbri, F. Bozza, T. Graule, I. E. Castelli, L. Wiles, N. Danilovic, K. E. Ayers, *et al.*, *Adv. Funct. Mater.*, 2018, **28**, 1804355.
42 W. T. Hong, M. Risch, K. A. Stoerzinger, A. Grimaud, J. Suntivich and Y. Shao-Horn, *Energy Environ. Sci.*, 2015, **8**, 1404–1427.
43 H. Over, Y. D. Kim, A. Seitsonen, S. Wendt, E. Lundgren, M. Schmid, P. Varga, A. Morgante and G. Ertl, *Science*, 2000, **287**, 1474–1476.
44 J. Kim, X. Yin, K.-C. Tsao, S. Fang and H. Yang, *J. Am. Chem. Soc.*, 2014, **136**, 14646–14649.
45 A. Grimaud, K. J. May, C. E. Carlton, Y.-L. Lee, M. Risch, W. T. Hong, J. Zhou and Y. Shao-Horn, *Nat. Commun.*, 2013, **4**, 2439.
46 A. Swarnkar, W. J. Mir and A. Nag, *ACS Energy Lett.*, 2018, **3**, 286–289.
47 W. Zhang, H. Liu, Y. Qu, J. Cui, W. Zhang, T. Shi and H.-L. Wang, *Adv. Mater.*, 2024, **36**, 2309193.
48 Y. Liang, F. Li, X. Cui, C. Stampfl, S. P. Ringer, X. Yang, J. Huang and R. Zheng, *Sci. Adv.*, 2025, **11**, eads7054.

49 Z. Li, P. Wei and G. Wang, *Energy Fuels*, 2022, **36**, 11724–11744.
50 C. E. Beall, E. Fabbri and T. J. Schmidt, *ACS Catal.*, 2021, **11**, 3094–3114.
51 S. Sen and T. K. Mandal, *ChemCatChem*, 2025, e00535.
52 J. T. Mefford, X. Rong, A. M. Abakumov, W. G. Hardin, S. Dai, A. M. Kolpak, K. P. Johnston and K. J. Stevenson, *Nat. Commun.*, 2016, **7**, 11053.
53 N. Zhang and Y. Xiong, *J. Phys. Chem. C*, 2023, **127**, 2147–2159.
54 B.-J. Kim, E. Fabbri, M. Borlaf, D. F. Abbott, I. E. Castelli, M. Nachtegaal, T. Graule and T. J. Schmidt, *Mater. Adv.*, 2021, **2**, 345–355.
55 L.-B. Liu, C. Yi, H.-C. Mi, S. L. Zhang, X.-Z. Fu, J.-L. Luo and S. Liu, *Electrochem. Energy Rev.*, 2024, **7**, 14.
56 Y. Ma, M. Zha, Y. Dong, L. Li and G. Hu, *Mater. Res. Express*, 2019, **6**, 115033.
57 Y.-F. Li and A. Selloni, *ACS Catal.*, 2014, **4**, 1148–1153.
58 F. Song, L. Bai, A. Moysiadou, S. Lee, C. Hu, L. Liardet and X. Hu, *J. Am. Chem. Soc.*, 2018, **140**, 7748–7759.
59 Z.-D. He, R. Tesch, M. J. Eslamibidgoli, M. H. Eikerling and P. M. Kowalski, *Nat. Commun.*, 2023, **14**, 3498.
60 I. Hussain, U. Sajjad, O. J. Kewate, U. Amara, F. Bibi, A. Hanan, D. Potphode, M. Ahmad, M. S. Javed, P. Rosaiah, *et al.*, *Mater. Today Phys.*, 2024, **42**, 101382.
61 H. Wang, W. Xu, S. Richins, K. Liaw, L. Yan, M. Zhou and H. Luo, *Electrochim. Acta*, 2019, **296**, 945–953.
62 H. Wang, J. Wang, Y. Pi, Q. Shao, Y. Tan and X. Huang, *Angew. Chem., Int. Ed.*, 2019, **131**, 2338–2342.
63 J. Bian, R. Su, Y. Yao, J. Wang, J. Zhou, F. Li, Z. L. Wang and C. Sun, *ACS Appl. Energy Mater.*, 2019, **2**, 923–931.
64 M. Bajdich, M. García-Mota, A. Vojvodic, J. K. Nørskov and A. T. Bell, *J. Am. Chem. Soc.*, 2013, **135**, 13521–13530.
65 O. N. Avcı, L. Sementa and A. Fortunelli, *ACS Catal.*, 2022, **12**, 9058–9073.
66 N. Karmodak and O. Andreussi, *J. Phys. Chem. C*, 2021, **125**, 10397–10405.
67 A. Li, S. Kong, C. Guo, H. Ooka, K. Adachi, D. Hashizume, Q. Jiang, H. Han, J. Xiao and R. Nakamura, *Nat. Catal.*, 2022, **5**, 109–118.
68 J. Suntivich, K. J. May, H. A. Gasteiger, J. B. Goodenough and Y. Shao-Horn, *Science*, 2011, **334**, 1383–1385.
69 A. S. Raman, R. Patel and A. Vojvodic, *Faraday Discuss.*, 2021, **229**, 75–88.
70 B. Luo, F. Li, K. Xu, Y. Guo, Y. Liu, Z. Xia and J. Z. Zhang, *J. Mater. Chem. C*, 2019, **7**, 2781–2808.
71 The computational details are in the SI.
72 G. Kresse and J. Hafner, *Phys. Rev. B: Condens. Matter Mater. Phys.*, 1993, **48**, 13115–13118.
73 G. Kresse and J. Furthmüller, *Phys. Rev. B: Condens. Matter Mater. Phys.*, 1996, **54**, 11169–11186.
74 G. Kresse and J. Furthmüller, *Comput. Mater. Sci.*, 1996, **6**, 15–50.
75 J. P. Perdew, K. Burke and M. Ernzerhof, *Phys. Rev. Lett.*, 1996, **77**, 3865.
76 S. Maintz, V. L. Deringer, A. L. Tchougréeff and R. Dronskowski, *J. Comput. Chem.*, 2013, **34**, 2557–2567.
77 G. Kresse and D. Joubert, *Phys. Rev. B: Condens. Matter Mater. Phys.*, 1999, **59**, 1758.
78 K. Mathew, R. Sundararaman, K. Letchworth-Weaver, T. Arias and R. G. Hennig, *J. Chem. Phys.*, 2014, **140**, 084106.
79 K. Mathew, V. Kolluru, S. Mula, S. N. Steinmann and R. G. Hennig, *J. Chem. Phys.*, 2019, **151**, 234101.
80 J. A. Gauthier, S. Ringe, C. F. Dickens, A. J. Garza, A. T. Bell, M. Head-Gordon, J. K. Nørskov and K. Chan, *ACS Catal.*, 2018, **9**, 920–931.
81 J. A. Gauthier, C. F. Dickens, S. Ringe and K. Chan, *ChemPhysChem*, 2019, **20**, 3074–3080.
82 O. Andreussi, I. Dabo and N. Marzari, *J. Chem. Phys.*, 2012, **136**, 064102.
83 A. H. Larsen, J. J. Mortensen, J. Blomqvist, I. E. Castelli, R. Christensen, M. Dułak, J. Friis, M. N. Groves, B. Hammer, C. Hargus, *et al.*, *J. Condens. Matter Phys.*, 2017, **29**, 273002.
84 Y. Choi, D. S. Mebane, M.-C. Lin and M. Liu, *Chem. Mater.*, 2007, **19**, 1690–1699.
85 R. Evarestov, E. Kotomin, Y. A. Mastrikov, D. Gryaznov, E. Heifets and J. Maier, *Phys. Rev. B: Condens. Matter Mater. Phys.*, 2005, **72**, 214411.
86 Y.-L. Lee, J. Kleis, J. Rossmeisl and D. Morgan, *Phys. Rev. B: Condens. Matter Mater. Phys.*, 2009, **80**, 224101.
87 L. Trotochaud, J. K. Ranney, K. N. Williams and S. W. Boettcher, *J. Am. Chem. Soc.*, 2012, **134**, 17253–17261.
88 J. O. Bockris and T. N. Veziroglu, *Int. J. Hydrogen Energy*, 2007, **32**, 1605–1610.
89 M. D. Bhatt and J. Y. Lee, *Energy Fuels*, 2020, **34**, 6634–6695.
90 R. Dronskowski and P. E. Bloechl, *J. Phys. Chem.*, 1993, **97**, 8617–8624.
91 S. Geiger, O. Kasian, M. Ledendecker, E. Pizzutilo, A. M. Mingers, W. T. Fu, O. Diaz-Morales, Z. Li, T. Oellers, L. Fruchter, *et al.*, *Nat. Catal.*, 2018, **1**, 508–515.
92 O. Kasian, J.-P. Grote, S. Geiger, S. Cherevko and K. J. Mayrhofer, *Angew. Chem., Int. Ed.*, 2018, **57**, 2488–2491.
93 C. W. Song, J. Lim, H. B. Bae and S.-Y. Chung, *Energy Environ. Sci.*, 2020, **13**, 4178–4188.
94 F.-Y. Chen, Z.-Y. Wu, Z. Adler and H. Wang, *Joule*, 2021, **5**, 1704–1731.
95 N. Zhang and Y. Chai, *Energy Environ. Sci.*, 2021, **14**, 4647–4671.
96 J. Zaanen, G. Sawatzky and J. Allen, *Phys. Rev. Lett.*, 1985, **55**, 418.
97 A. Grimaud, W. T. Hong, Y. Shao-Horn and J.-M. Tarascon, *Nat. Mater.*, 2016, **15**, 121–126.
98 W. Zhang, Y. Wang, Y. Li and X. Zhang, *J. Ind. Eng. Chem.*, 2024, **139**, 199–212.
99 S. R. Ede, C. N. Collins, C. D. Posada, G. George, H. Wu, W. D. Ratcliff, Y. Lin, J. Wen, S. Han and Z. Luo, *ACS Catal.*, 2021, **11**, 4327–4337.
100 S. Razzaq and K. S. Exner, *ACS Catal.*, 2023, **13**, 1740–1758.
101 K. S. Exner, *ACS Catal.*, 2020, **10**, 12607–12617.
102 M. Usama, S. Razzaq, C. Hättig, S. N. Steinmann and K. S. Exner, *Nat. Commun.*, 2025, **16**, 6137.
103 K. Dhaka and K. S. Exner, *J. Catal.*, 2025, **443**, 115970.